



HAL
open science

Developments of the time-domain impedance boundary condition for combustion problems

Remi Roncen, Jose Cardesa Duenas, Thomas Marchal

► To cite this version:

Remi Roncen, Jose Cardesa Duenas, Thomas Marchal. Developments of the time-domain impedance boundary condition for combustion problems. SoTiC (Symposium on Thermoacoustics in Combustion: Industry meets Academia) 2023, Sep 2023, Zurich, Switzerland. hal-04187365v2

HAL Id: hal-04187365

<https://hal.science/hal-04187365v2>

Submitted on 7 Nov 2023

HAL is a multi-disciplinary open access archive for the deposit and dissemination of scientific research documents, whether they are published or not. The documents may come from teaching and research institutions in France or abroad, or from public or private research centers.

L'archive ouverte pluridisciplinaire **HAL**, est destinée au dépôt et à la diffusion de documents scientifiques de niveau recherche, publiés ou non, émanant des établissements d'enseignement et de recherche français ou étrangers, des laboratoires publics ou privés.

Developments of the time-domain impedance boundary condition for combustion problems

Rémi Roncen¹, José I. Cardesa¹ and Thomas Marchal²

Abstract

Thermoacoustic instabilities can cause significant pressure oscillations and potentially lead to the failure of combustion systems. These instabilities result from the interaction between heat release fluctuations and acoustic waves. One potential solution to mitigate thermoacoustic instabilities is to use passive acoustic damping devices, referred to as liners. These liners absorb acoustic waves and aim to break the instability loop. To represent such materials in time domain solvers, a complex impedance convolution problem must be solved. In this work, we describe a recently implemented time-domain impedance boundary condition, with extended capabilities that make it a promising candidate for combustion solvers.

Keywords

Impedance, Scattering, Dynamic impulse response, TDIBC, Broadband, Non-linear, Spectral difference, Combustion, Instabilities

Introduction

Thermoacoustic instabilities are complex phenomena that are pervasive to combustion systems such as gas turbines, rocket engines and furnaces (1–3). These instabilities are caused by the interaction between combustion processes and the acoustic field (4), leading to dangerous pressure oscillations that can damage equipment and compromise safety (5). Acoustic waves are the primary drivers of these thermoacoustic instabilities (3; 6), and are strongly influenced by the system's upstream and downstream boundary conditions.

In the field of aeroacoustics, passive wall treatments called liners are used in engine nacelles to suppress noise propagation. These liners are usually composed of assemblies of perforated sheets bonded onto honeycomb cavities, and operate on the principle of resonators. The introduction of liners in combustion chambers was shown to help reduce the feedback loop responsible for thermoacoustic instabilities, via a wave absorption mechanism (7–18). In both aeroacoustics and combustion applications, the fundamental characteristic of liners is the surface impedance, which is a frequency transfer function between the acoustic pressure and the acoustic particle velocity normal to the liner (19).

When relying on high fidelity numerical simulations to predict the fluid flow behavior and the acoustics of a system, impedance boundary conditions (IBCs) provide a convenient tool to replace some elements of the geometry, allowing the simulation domain to be truncated. Such elements not only include the perforations and cavities of a liner, but also parts of the injection system and any complex system downstream or upstream the combustion chamber, which play an important role in the acoustic response of the system (20).

While impedance modeling of acoustic liners was initially conducted in the frequency domain, most combustion solvers rely on solving time-domain equations. In recent decades, there has been significant progress in the development of time-domain impedance boundary conditions (TDIBC), which have demonstrated their ability to target more or less broadband behaviors and to handle nonlinear impedance operators (21–25). The majority of these techniques rely on approximating the complex, frequency-dependent impedance operator with rational functions.

The present paper focuses on another type of method based on the liner impulse response (IR), introduced in (25), and extends its capabilities in order to alleviate one of the method's limitations linked to the small time step used in numerical combustion problems. It was implemented in a high-order Spectral Difference (SD) solver and validated on non-reacting test cases (25). Recently, this same solver was extended to multispecies reacting flows, showing equivalent results with classical combustion solvers (26). It was the first time that the SD method was used in a combustion context, showing its capability to handle such complex flows. A key feature of the present work is the combined use of both multispecies combustion and IR-TDIBCs within the same SD-based Navier-Stokes flow solver.

The structure of the paper is as follows. First, impedance modeling is briefly summarized, and the IR-TDIBC approach is presented with its additional features over classical TDIBCs. A 2D methane-air burner is then

¹ ONERA, Département Multi-Physique pour l'Énergétique, Université de Toulouse, F-31055, Toulouse, France, ² Computational Fluid Dynamics Team, CERFACS, Toulouse, 31057, France

Corresponding author:
Rémi Roncen, ONERA/DMPE
Email: remi.roncen@onera.fr

considered using the SD solver for the compressible reacting Navier-Stokes equations, wherein the IR-TDIBC condition is incorporated within the injector section. This setup is designed to demonstrate how the IR-TDIBC condition impacts the pressure fields within the combustor, as well as to investigate the implementation details within a reactive solver. Conclusions are then drawn, with a focus on future developments.

Aeroacoustic liners

This section provides an overview of aeroacoustic liners and their acoustic modeling. The focus is placed on the simplest (and most widely used) liner concept, but the interested reader can refer to Ref. (27) for a more thorough discussion including novel liner concepts.

Aeroacoustic liners are acoustic-absorbing materials strategically placed to mitigate noise produced by various types of systems, including turbofan engines. The most used liner to date is the single degree of freedom (SDOF) liner, consisting in a perforated plate placed on top of cavities, backed by a rigid plate. Relying on a resonance effect to increase the acoustic particle velocity in the vicinity of the perforated plate at given frequencies, viscous dissipation can be greatly increased, thus leading to efficient acoustic damping. A schematic of such an SDOF liner is given in Figure 1. Some physical phenomena having a role in determining the acoustic response of aeroacoustic liners are also displayed in Figure 1. In the particular field of combustion instabilities and their damping, one notes the presence of a shear grazing flow (potentially shocked in scramjet engines), a cooling bias flow used to sheath the wall from high temperatures, high amplitude acoustic waves (potentially nonlinear) and large temperature gradients in the cavities. Note that the temperature gradient displayed here is related to a combustion chamber configuration. The gradient is reversed in a turbofan engine within the nacelle, where hot anti-icing devices are placed near the rigid backing plate, and the grazing flow is cold.

Impedance modeling

In the frequency domain, locally-reacting acoustic liners are defined by their *normalized* surface impedance, denoted by the complex frequency-dependent quantity \tilde{Z} . The impedance of a liner represents the transfer function between acoustic pressure and normal velocity at the liner surface $\tilde{Z} = \tilde{p} / (z_0 \tilde{\mathbf{u}} \cdot \mathbf{n})$, where \tilde{p} is the acoustic pressure, $\tilde{\mathbf{u}} \cdot \mathbf{n}$ is the normal acoustic velocity at the liner surface, and z_0 is the characteristic impedance of air, i.e., the product of speed of sound and density.

The impedance is not always a convenient quantity to treat within numerical codes, due to its unbounded nature. The scattering operator $\tilde{\mathcal{R}}$, which describes the ratio of the reflected wave to the incident wave, is a more practical way to work with liners: $\tilde{\mathcal{R}} = (\tilde{Z} - 1) / (\tilde{Z} + 1)$. Perforated plates can be approximated as porous foams, simplifying their modeling, and the transfer matrix approach can determine the global surface impedance of an assembly by multiplying the matrices of each layer sequentially. The paper's objective is not to provide a detailed model for the

impedance of a liner, but rather to develop a model-agnostic TDIBC that requires no parameter fitting. For pedagogical purposes, this section presents the normalized impedance for a single degree of freedom (SDOF) liner based on Atalla and Sgard's model (28):

$$\tilde{Z}_{\text{SDOF}}(\omega) = \frac{R_s}{c_f \phi_p} \left(\frac{2L_p}{r_p} + 4 \frac{\epsilon_e}{r_p} \right) (1 + j) + \frac{1}{c_f \phi_p} (2\epsilon_e + L_p) j\omega + \frac{1}{\phi_c} \coth(j\tilde{k}_c L_c) \quad (1)$$

$$\epsilon_e = 0.85 r_p \left(1 - 1.14 \sqrt{\phi_p} \right) \quad (2)$$

$$R_s = \frac{1}{2} \sqrt{2\eta\omega\rho_f} \quad (3)$$

$$j\tilde{k}_c = \frac{j\omega}{c_f} \left[\frac{1 + (\gamma - 1) \Phi(k_\kappa r_c)}{1 - \Phi(k_\kappa r_c)} \right]^{1/2} \quad (4)$$

$$\Phi(s) = \frac{2}{s} \frac{I_1}{I_2}(s). \quad (5)$$

In the previous equations, L_p is the thickness of the perforated face sheet, ϕ_p its porosity, r_p the radius of its perforations. Similarly, L_c , ϕ_c and r_c define the honeycomb cavity properties. The ambient air is defined by its speed of sound c_f , density ρ_f , the ratio of specific heat constants γ , the dynamic viscosity η , the cinematic viscosity ν and the thermal conductivity κ . The modified Bessel functions of the first kind of order n are written I_n , and $k_\nu = \sqrt{j\omega/\nu}$, $k_\kappa = \sqrt{j\omega/\kappa}$.

Non-linear modeling

Combustion chambers subject to instabilities are typically sustaining high sound pressure levels (SPLs), which can lead to nonlinear impedance effects in perforated liners. These nonlinear effects relate to a vortex-shedding mechanism near the perforations, which changes the liner's response to acoustic waves, and thus its impedance. Models for liner nonlinearity typically involve a nonlinear function of the acoustic particle velocity just outside the perforation, for instance with the Guess model (29) as

$$\tilde{Z}_{\text{NL}} = \tilde{Z} + \alpha_{\text{NL}} |v|, \quad (6)$$

where v is the acoustic particle velocity *just outside* the perforation, and α_{NL} is a parameter describing how nonlinear the liner response is (see e.g. Refs.(29; 30)). While not taken into account explicitly in the following, both the shear grazing flow and the bias flow can have an influence on the impedance, primarily on its real part. The interested reader can refer to (13) for more details on the topic, in relation to combustion chamber liners.

Direct convolution approach in time domain

In this section, the concept of IR-TDIBC is re-introduced, following the developments of Ref. (25), where the implementation is detailed, and where python scripts are made available to help the reader become familiar with the method.

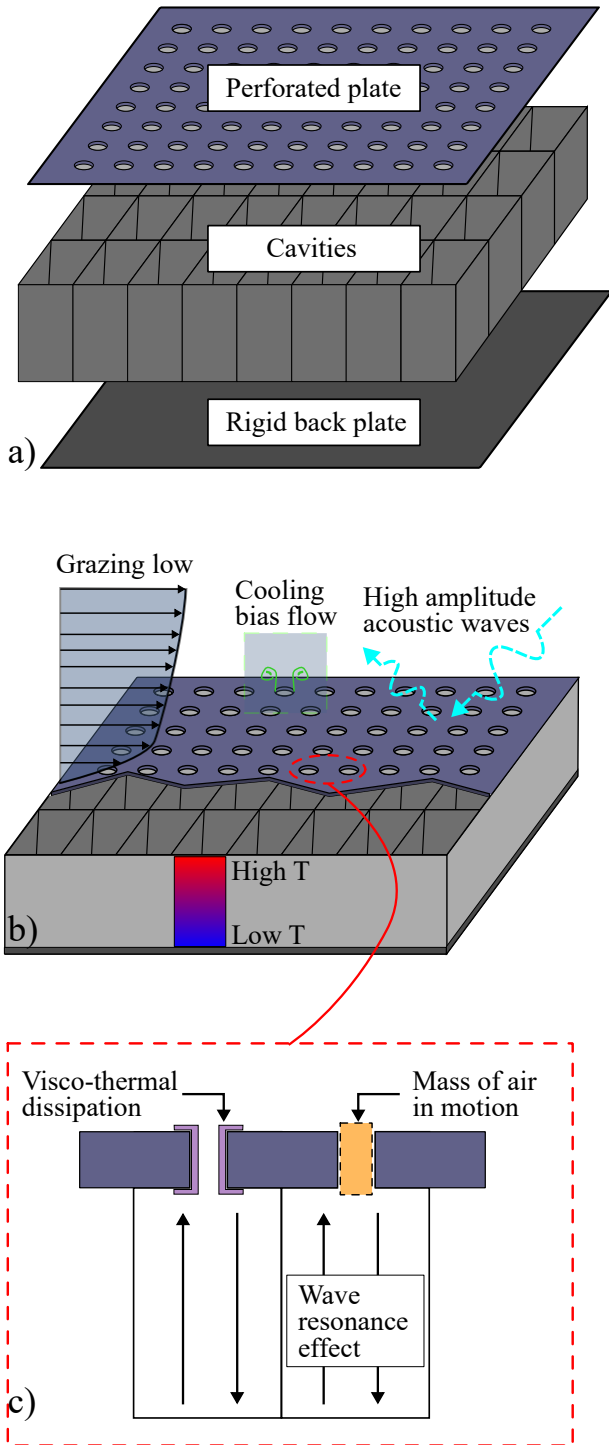


Figure 1. a) Exploded view of an SDOF liner. b) Multiple physical mechanisms at play when determining the acoustic response of an SDOF. c) Focus on the basic effects responsible for acoustic absorption.

Impulse response TDIBC

Linear convolution Using a linear impedance BC in time domain amounts to solving a linear time invariant (LTI) system. Let $x(t)$ be an input wave signal and $y(t)$ the output wave. In the linear case, one needs to solve

$$y(t) = x(t) * \mathcal{R}(t),$$

$$y(t) = \int_0^{+\infty} x(\tau) \mathcal{R}(t - \tau) d\tau, \quad (7)$$

where the IR operator $\mathcal{R}(t)$ can be obtained by Fourier transform of the known scattering coefficient $\tilde{\mathcal{R}}$. This IR corresponds to the response of the system to a Dirac pulse, and the input $x(t)$ can be considered as a series of appropriately scaled Dirac pulses, so Eq. (7) can be approximated at time t_N as

$$y(t_N) = \sum_{n \in [0, N]} x(t_n) \mathcal{R}(t_N - t_n), \quad (8)$$

where $t_n = n \times dt$, with $dt > 0$ being the simulation time step.

Evidently, in a numerical solver, one does not know the entire input $x(t)$ in advance, which makes the direct application of Eq. (7) unfeasible.

At the root of the present method is a simplified input-output representation of the TDIBC: at each time step of a numerical solver, the TDIBC is given an input that is a Dirac pulse with a certain amplitude, i.e., the amplitude of the incoming acoustic wave. Using the IR in the form of an array, one can efficiently store the future response of the TDIBC to this Dirac pulse. By means of the linearity property of the convolution operator, one can incrementally update this future response at every time step by simply adding the IR to the current storage array entry, which then needs to be shifted by one element to be sent back as an output of the TDIBC.

To give a sense of how the IR-TDIBC handles different signals, Figure 2 showcases the signal output, $y(t)$, representing the wave reflected by the IR-TDIBC for three distinct signal inputs, $x(t)$. Numerical simulations, such as those performed by CFD solvers, treat input signals as discrete sets of values. In the case of the IR-TDIBC, each of these discrete values is treated individually, akin to Dirac functions, and their contributions are successively integrated without imposing any additional burden on the IR-TDIBC memory storage. This efficient approach ensures accurate representation and effective handling of various input signals within the TDIBC framework, including discontinuous ones. This property could prove useful in configurations with shock waves.

We argue that the IR-TDIBC method is intrinsically more broadband than the numerical scheme used for the simulation, that it is capable of representing even the most complex liner combinations (meta materials) with ease, and that it can readily handle nonlinear input signals. In addition, it requires no fitting on the user part, only an extensive knowledge of the frequency-domain reflection coefficient or the surface impedance.

The claim of broadbandness for the IR-TDIBC stems from its ability to handle waves of frequency up to $0.5/dt$. This is in contrast with CFD solvers, even high-order ones, where the dispersion and diffusion free propagation of an acoustic wave is linked to mesh density and scheme order, often requiring many degrees of freedom per wavelength. The stability condition of the simulation enforces a relationship between mesh size and time step, via the CFL number. As a result, only waves of frequency up to ϵ/dt can be handled correctly, with $\epsilon \leq 0.5$.

Non-linear convolution

In the case where the impedance is considered to have a dependency on the acoustic particle velocity, which is

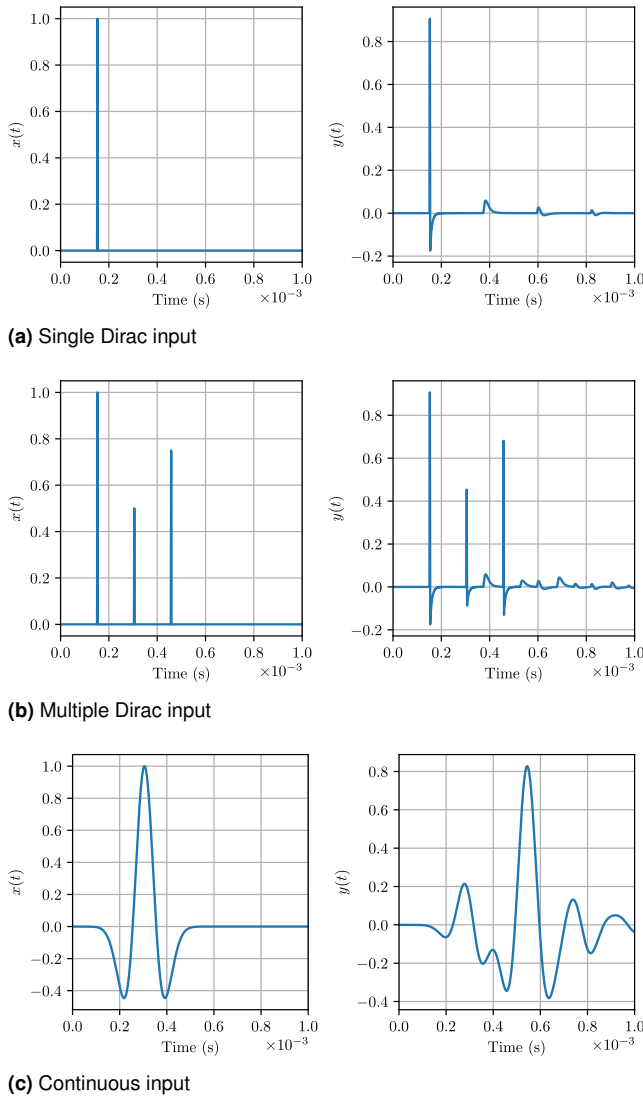


Figure 2. Examples of signals reflected by the IR-TDIBC (right), for different input signals (left).

standard in SDOF liners used for passive absorption, one has to dynamically update the impulse response. Using an impulse response switching, the LTI system in Eq. (8) is transformed and becomes

$$y(t_N) = \sum_{n \in [0, N]} x(t_n) \mathcal{R}(t_N - t_n, v(t_N - t_n)). \quad (9)$$

Instead of having to recalculate the impulse response at each time step for a given wave amplitude, our implementation in numerical codes relies on an interpolation of the IR as a function of the particle velocity v . Note that this particle velocity in the perforation is obtained simply by conservation of mass, knowing the particle velocity outside the TDIBC and the porosity of the perforated sheet being modeled.

We note in passing that all TDIBC methods share a common physical limitation where the future of a wave that has entered the liner becomes fixed. In experiments, when the wave returns to the perforated sheet after having been reflected at the bottom of the cavity, its behavior can be influenced again by the nonlinear characteristics at the perforation as it exits. This aspect is beyond the prediction

capability of the current method, and might still be only possible through the use of resolved simulations such as large eddy simulations (LES), where each perforation and cavity is meshed. As shown next in the validation Section, the pointed out lack of memory might have no significant impact on the modeling outcome in practice.

Validation

In order to validate the described method, two experiments conducted at NASA were reproduced numerically using a simplified solver where only time domain integration was conducted. In addition, nonlinear effects from the samples being tested were accounted for, thus reproducing the experimental conditions of SPL in an impedance tube – see the schematic given in Figure 3. The nonlinear parameter α_{NL} is taken as $(1 - \phi_p^2)/(c_f \phi_p^2)$.

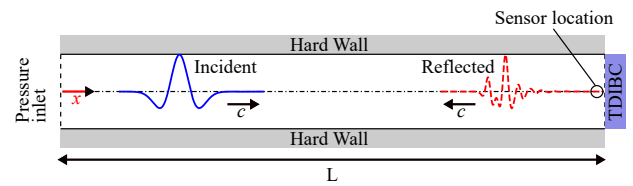


Figure 3. Setup of the impedance tube test case. A right-running pressure wave enters the domain at $x = 0$ and impacts the TDIBC at $x = L$, where it is reflected back towards the inlet.

The absorption coefficients obtained from time-domain signals using the IR-TDIBC are shown in Figure 4 for sample GE01 (a SDOF liner of facesheet porosity 8.7%, facesheet thickness 0.635 mm and diameter of perforations 1 mm, and a total thickness of 38.1 mm). A very good agreement is obtained in Figure 4, validating the method's implementation, as well as giving support to the simplifications resulting from the nonlinear consideration of the impulse response (the impedance was also shown to correctly fit the reference data).

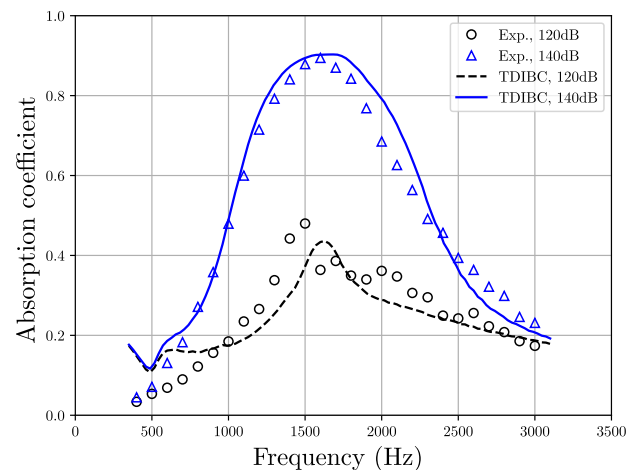


Figure 4. Absorption of the GE01 sample, comparison between NASA's experiments and the present IR-TDIBC model.

Asynchronicity of the IR-TDIBC

A common problem encountered in most combustion solvers using explicit time integration is the high stiffness of the

numerical and chemical schemes employed. This results in very low time steps. A first drawback in having such a low time step is of course that one has to “call” more often the TDIBC solver. An additional drawback linked to low time steps that is specific to the IR-TDIBC follows from the time-frequency relationship: reducing the time step of the simulation leads to an increase in the frequency step of the represented operator – here the reflection coefficient. This means that for a given memory allocation of the IR in a storage array, one obtains a coarser representation, in frequency, of the modeled operator. An idea that was suggested in passing in Ref. (25) was to asynchronously the IR-TDIBC with respect to the main flow solver. The justification for doing so is that time scales associated with acoustics are orders of magnitude greater than those required by the combustion processes. A higher time step for the IR-TDIBC could solve two issues at once: fewer calls required, thus decreasing the numerical cost, and a finer frequency-step obtained at a lesser memory cost.

The asynchronous implementation differs from the synchronous one, since the input is averaged over a moving window. First results are given in Figure 5, where the reflected wave is displayed in time domain. A Gaussian pulse was sent on the IR-TDIBC, representing the GE01 sample, and the reflected wave was recorded and compared to the reference (obtained by direct convolution with the entire known input $x(t)$). The reference time step is $1.5 \cdot 10^{-7} s$, in line with some small time steps encountered in industrial codes for combustion or aeroacoustics (they can become much lower depending on the CFL condition imposed in the solver). By increasing the asynchronicity, i.e., the integer N_{async} that determines the number of time steps between two updates of the IR-TDIBC, a step-wise “aliasing” behavior of the reflected wave appears, as well as a time lag equal to $N_{\text{async}} \times dt$. For a much smaller simulation time step, one could increase N_{async} even more without any visible aliasing.

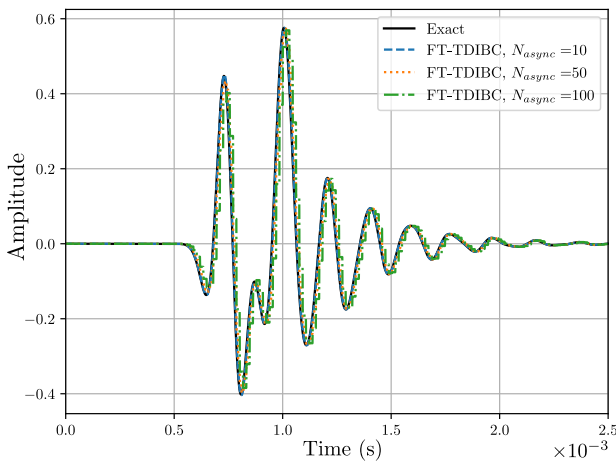


Figure 5. Reflected wave obtained for different asynchronous levels of the IR-TDIBC, for the GE01 sample.

Uncertainty quantification with the IR-TDIBC

An important aspect of CFD is how to address uncertainties in fluid flow simulations, especially in combustion modeling, where errors can lead to severe safety risks (predicting a

stable combustion while it is actually unstable). Uncertainty Quantification (UQ) serves vital purposes, such as enhancing prediction reliability, validating and calibrating models, enabling robust system design, reducing costs and aiding risk assessment.

UQ techniques fall into two families: intrusive, which modifies equations directly for efficient and accurate uncertainty estimation; and non-intrusive, which uses Monte-Carlo sampling methods and can be computationally expensive for high-dimensional problems. Intrusive methods offer computational advantages for complex simulations, making them valuable for certain UQ applications.

Although these authors are not aware of existing solvers tackling intrusive UQ with combustion, it is worth mentioning that the current IR-TDIBC method could readily be suitable to such solvers, owing to its additive properties. To showcase this feature, an uncertain signal is considered. The geometrical properties of aeroacoustic liners are also considered uncertain, which represents manufacturing defects. The previous considerations lead to a credibility interval on the impulse response representing the GE01 sample, an SDOF liner. Both the input signals and the IR are assumed normally distributed, and the IR-TDIBC algorithm is augmented to account for both the mean and the standard deviation of the signals. The input IR and output signals are presented in Figure 6, where only the linear case was treated. Dealing with the liner nonlinear behavior using UQ is a direction for future work, which needs to be conducted together with the development of solvers capable of effectively integrating such boundary conditions.

Testing the IR-TDIBC in a 2D reactive-flow

The JAGUAR solver for reactive flows

Governing equations The IR-TDIBC implementation was performed in JAGUAR (26; 31–35), a SD solver for the 3D reacting compressible Navier-Stokes equations (NSE) developed by CERFACS and ONERA. The SD method (36) is a high-order discontinuous method for spatial discretization which approximates conservative variables and their fluxes with two polynomials of degree p and $p + 1$, respectively, allowing for high-order discretization on unstructured meshes for complex geometries. In this work, the 2D reacting compressible NSE for a multispecies gas composed of N_s species are considered:

$$\frac{\partial \mathbf{U}}{\partial t} + \frac{\partial \mathbf{E}}{\partial x} + \frac{\partial \mathbf{F}}{\partial y} = \mathbf{S} \quad (10)$$

where $\mathbf{U} = (\rho, \rho u, \rho v, \rho E, \rho Y_k)^T$ is the vector of conservative variables with ρ the density of the mixture, u (respectively v) the velocity component along the x -axis (respectively y -axis), E the total non-chemical energy per unit mass and Y_k the mass fraction of species $k \in \llbracket 1, N_s \rrbracket$. Additionally in Eq. (10), $\mathbf{E} = \mathbf{E}_c + \mathbf{E}_d$ and $\mathbf{F} = \mathbf{F}_c + \mathbf{F}_d$ are respectively the sum of convective and diffusive fluxes of \mathbf{U} along x and y directions. \mathbf{S} is a source term vector containing the heat release rate and the net chemical production rates of each species. Expressions of $\mathbf{E}_{c/d}$, $\mathbf{F}_{c/d}$ and \mathbf{S} used in the JAGUAR solver can be found in (26). The species diffusive flux uses the Hirschfelder and Curtiss

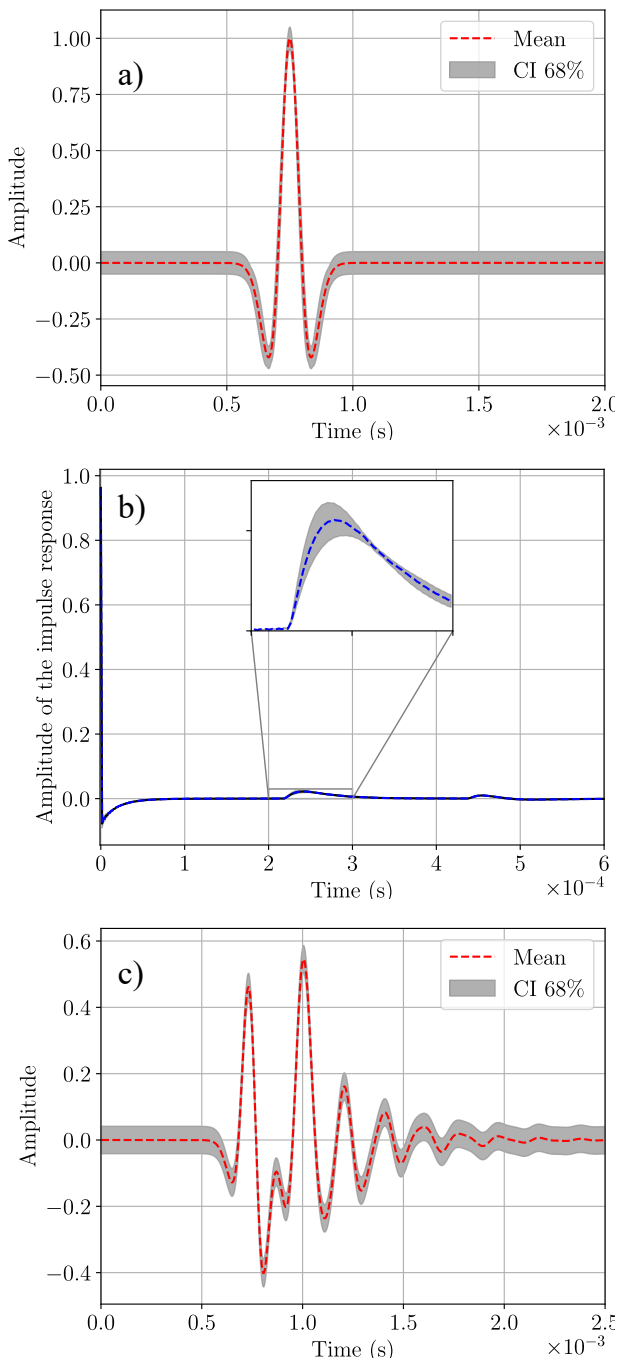


Figure 6. Considerations of UQ with the IR-TDIBC. CI = credibility interval. a) Input signal and uncertainties. b) Impulse response of the GE01 sample and uncertainties, associated with a 5% uncertainty on the material physical parameters. c) Output signal and uncertainties, obtained in a single simulation.

approximation along with a constant Schmidt number for each species (37). Species enthalpies are computed from JANAF enthalpy tables (38), and the mixture is assumed to behave like an ideal gas.

Principle of the SD discretization on quadrilateral elements for reacting flows Given a computational domain Ω divided into N_e non-overlapping quadrilateral elements inside which Eq. (10) is to be solved, the SD method transforms each element Ω_e of Ω into a standard quadrilateral $\mathcal{Q}_e = \{(\xi, \eta), 0 \leq \xi, \eta \leq 1\}$ following an isoparametric transformation characterized by a Jacobian matrix J .

Equation (10) is then recast in the standard domain \mathcal{H}_e as (39):

$$\frac{\partial \hat{\mathbf{U}}}{\partial t} + \frac{\partial \hat{\mathbf{E}}}{\partial \xi} + \frac{\partial \hat{\mathbf{F}}}{\partial \eta} = \hat{\mathbf{S}} \quad (11)$$

with

$$\begin{pmatrix} \hat{\mathbf{E}} \\ \hat{\mathbf{F}} \end{pmatrix} = |J|J^{-1} \cdot \begin{pmatrix} \mathbf{E} \\ \mathbf{F} \end{pmatrix}, \quad \hat{\mathbf{U}} = |J|\mathbf{U}, \quad \hat{\mathbf{S}} = |J|\mathbf{S} \quad (12)$$

where $|J|$ is the determinant of J . The SD method builds $\hat{\mathbf{U}}$ as a p -degree polynomial inside \mathcal{Q}_e using its known values at what are called solution points (SP), whereas $\hat{\mathbf{E}}$ and $\hat{\mathbf{F}}$ are built as $(p+1)$ -degree polynomials at another set of points called flux points (FP). The resulting spatial discretization is of order $p+1$. Along each direction there are $p+1$ SP and $p+2$ FP. The SP are always strictly inside \mathcal{Q}_e and are set here as the Gauss-Chebyshev points of the first kind defined in (39), whereas the FP contain the element boundaries 0 and 1 plus the p Gauss-Legendre quadrature points for stability reasons (40; 41). Following (26), for a multispecies gas simulated with the SD method, we chose the set of primitive variables as (T, u, v, P, Y_k) , where T is the temperature and P the static pressure. These variables are interpolated from SP to FP and are then used to compute fluxes at FP. At element interfaces, both convective and diffusive fluxes are discontinuous, so interface numerical fluxes have to be computed to ensure the conservation of the numerical scheme. For the convective fluxes, a Riemann solver (42) is commonly employed and in this work the Harten Lax and van Leer Contact (HLLC) scheme (43) is considered. For the diffusive fluxes, a centered scheme, as firstly proposed in (26), is used. Once internal and interface fluxes have been computed at all FP, flux derivatives are evaluated at SP and Eq. (11) is marched in time using any explicit temporal scheme, at each SP inside all elements. In this work, the three-stage third-order in time strong stability preserving Runge-Kutta scheme of Gottlieb and Shu (44) is employed, with a constant CFL number of 0.3.

The methane-air burner configuration

Geometry and boundary conditions In order to use the IR-TDIBC in a reacting simulation, a 2D methane-air burner is considered. The geometry is the same as the one used in (26) but it has a much longer injector length as shown in Figure 6 where the injector goes from $x = 0$ to $x = 50$ mm (instead of 10 mm in (26)). The chemical mechanism is the two-reactions CH₄/Air-2S-BFER developed by Franzelli *et al.* (45) which is composed of six species (CH₄, O₂, N₂, H₂O, CO and CO₂) reacting through two chemical reactions. Fresh gases are premixed and enter the burner axially through a Navier-Stokes Characteristic Boundary Condition (NSCBC (46)) subsonic inflow at $x = 0$ imposing:

- an axial parabolic velocity profile

$$u(y) = u_0 \left(1 - \frac{y^2}{l_0^2}\right), \quad v = 0 \quad (13)$$

with $u_0 = 4 \text{ m}\cdot\text{s}^{-1}$ and $l_0 = 0.65 \text{ mm}$.

- a fresh gas temperature $T = 300 \text{ K}$.

- species mass fractions of the fresh gases in order to have an equivalence ratio of 0.8 that is: $Y_{\text{CH}_4} = 0.0446$, $Y_{\text{O}_2} = 0.2226$ and $Y_{\text{N}_2} = 0.7328$.

The outlet at $x = 70$ mm is modeled with an NSCBC subsonic outflow imposing $P = 101325$ Pa. Two IR-TDIBC liners are located from $x = 10$ mm to $x = 40$ mm at respectively $y = -l_0$ and $y = l_0$. Remaining walls inside the injector are modeled as adiabatic no-slip walls. Finally, symmetry boundary conditions are employed for side walls inside the combustion chamber. The way of imposing NSCBC and TDIBC within the SD formalism is described in more details in (26; 35).

Mesh discretization The computational domain is discretized using $N_e = 1912$ uniform quadrilateral elements of characteristic size $\Delta_e = 0.325$ mm and the polynomial degree within each of them is set to $p = 4$ (fifth-order scheme). This discretization ensures at least eight points inside the flame front, which is sufficient to resolve it correctly.

Results and discussion A first simulation is run for 100 ms of physical time to obtain a stabilized flame in the burner. Following that, two additional simulations are run for another 100 ms, both starting from the end of the first simulation. In simulation A, no IR-TDIBC is present, while it is activated in simulation B. In both simulations A and B, a multi-sine wave excitation is superimposed to the main axial flow at the inlet, with frequencies f_i ($f_1 = 8.5$ kHz, $f_2 = 17$ kHz, $f_3 = 34$ kHz, and $f_4 = 68$ kHz).

The goal of this multi-sine excitation is to mimic an instability to demonstrate the effect of the IR-TDIBC. For simplicity, the impedance related to the IR-TDIBC is assumed constant over the entire frequency range and set to $\tilde{Z} = 1$. This corresponds to a fully absorbent material when the wave has an incidence normal to the material surface. Although the present simulation has grazing incidence and flow, conditions that deviate from absorption optimality, we still expect strong absorption. The impulse response of the reflection coefficient is 0 at all time steps, which reduces the storage cost associated with the IR-TDIBC. An array of size 2 is enough to conduct the iterative convolution presented in Eq. (8).

It is important to note that the present case is of limited practical interest concerning combustion instabilities due to the targeted frequency range and the simplicity of the selected impedance, which is unfeasible over the entire frequency range by any material known to the authors. However, our intention with this case was to demonstrate feasibility and test our implementation of the IR-TDIBC in a reactive flow solver.

A synthesis of the obtained results is given in Figure 7, where the heat release rate and pressure fields are displayed for simulation B (with the IR-TDIBC). Additionally, a plot of the acoustic pressure along the x -axis is shown, exhibiting a rapid decrease in wave amplitude as the wave grazes the IR-TDIBC. Finally, we integrate spatially over the source term of the energy equation in Eq. (10) at each time step. This integration yields the energy spectrum $\tilde{\mathcal{E}}$ displayed in Figure 7.d) after recording the integral over time (100 ms). As expected, in the case of simulation A where no IR-TDIBC is present (rigid walls are used everywhere), the spectrum

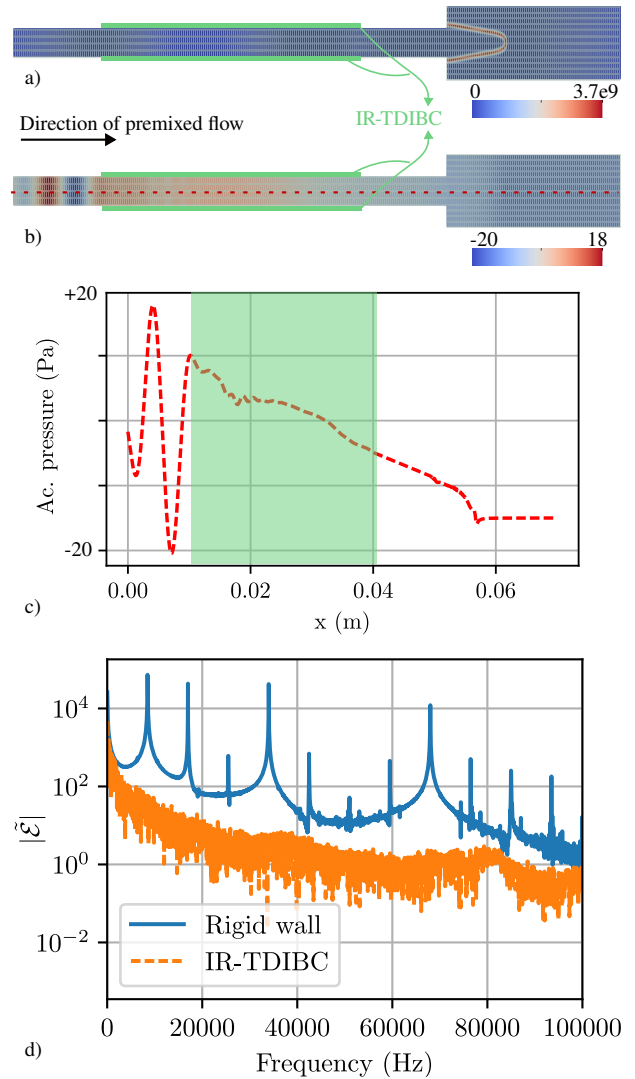


Figure 7. Overview of the burner numerical case. a) Heat release rate field ($\text{J}/\text{m}^3/\text{s}$). b) Acoustic pressure field (Pa). c) Acoustic pressure along the x -axis (Pa), with the IR-TDIBC range shown in green. d) Amplitude of the total energy spectrum shown in the entire domain.

displays large amplitudes at the frequencies corresponding to the multi-sine excitation. This indicates that the waves have impinged on the flame and modulated its surface, resulting in high non-steady oscillations of the flame front and thus the heat release rate. In contrast, with the IR-TDIBC present, the waves are sufficiently damped to not perturb the flame front anymore, leading to a total absence of any peaks in the spectrum.

As an important side note, we remark that the overall CPU-time was almost identical for both simulations A and B, with a negligible speed-up when the IR-TDIBC was used (the difference remained within cluster variations). Increasing the complexity of the IR and considering a 10^4 elements in the convolution-array led to a 13% slow-down of simulation B. Note that the asynchronous condition has not yet been implemented in JAGUAR. Additionally, no optimization of this new part of the code was performed yet, so it is expected that improvements in terms of speed could be obtained in the future.

Conclusions and future work

The correct representation of acoustic systems in time domain requires an accurate handling of both aeroacoustic liners and termination conditions. Focusing on the former, this paper introduced to the combustion community a TDIBC method based on the impulse response representation (25). The IR-TDIBC efficiently handles broadband and nonlinear acoustic behaviors, making it promising for combustion solvers. Validation against experimental data demonstrated its accuracy in representing aeroacoustic liners impedance. Augmenting our previous work, we introduced the asynchronous implementation of the IR-TDIBC, which proved effective in mitigating the computational burden, making it applicable in high-stiffness reactive flow solvers. Additionally, the method's potential for UQ was showcased, offering some insights for future combustion modeling that could rely on intrusive numerical solvers for uncertainty propagation. To test the IR-TDIBC in a reactive flow solver, the JAGUAR code was used to represent a methane-air burner in 2D. The walls of the injector were partly replaced by the IR-TDIBC, displaying the attenuation in pressure wave expected from this configuration, as well as a drastic reduction in the heat release rate oscillations of the flame, which was not subject to perturbations anymore. Future work will focus on addressing more complex configurations that naturally exhibit instabilities, such as the afterburner configuration studied in Ref. (47). In this context, the advantageous use of IR-TDIBC could provide valuable insights into the optimal placement of aeroacoustic liners.

Acknowledgments

The authors express their gratitude to Riwan Hammachi and Hugues Deniau for their constructive discussions and continuous assistance in the integration of the IR-TDIBC within the JAGUAR solver.

References

- [1] Barrere M and Williams FA. Comparison of combustion instabilities found in various types of combustion chambers. In *Symposium (International) on Combustion*, volume 12. Elsevier, pp. 169–181. DOI:10.1016/S0082-0784(69)80401-7.
- [2] Candel SM. Combustion instabilities coupled by pressure waves and their active control. In *Symposium (International) on Combustion*, volume 24. Elsevier, pp. 1277–1296. DOI: 10.1016/S0082-0784(06)80150-5.
- [3] Dowling AP. The calculation of thermoacoustic oscillations. *Journal of sound and vibration* 1995; 180(4): 557–581. DOI: 10.1006/jsvi.1995.0100.
- [4] Lieuwen T. Modeling premixed combustion-acoustic wave interactions: A review. *Journal of propulsion and power* 2003; 19(5): 765–781. DOI:10.2514/2.6193.
- [5] Ducruix S, Schuller T, Durox D et al. Combustion dynamics and instabilities: Elementary coupling and driving mechanisms. *Journal of propulsion and power* 2003; 19(5): 722–734. DOI:10.2514/2.6182.
- [6] Dowling AP and Stow SR. Acoustic analysis of gas turbine combustors. *Journal of propulsion and power* 2003; 19(5): 751–764. DOI:10.2514/2.6192.
- [7] Eldredge JD and Dowling AP. The absorption of axial acoustic waves by a perforated liner with bias flow. *Journal of Fluid Mechanics* 2003; 485: 307–335. DOI:10.1017/S0022112003004518.
- [8] Tran N, Ducruix S and Schuller T. Analysis and control of combustion instabilities by adaptive reflection coefficients. In *13th AIAA/CEAS Aeroacoustics Conference (28th AIAA Aeroacoustics Conference)*. p. 3716. DOI:10.2514/6.2007-3716.
- [9] Tran N, Ducruix S and Schuller T. Passive control of the inlet acoustic boundary of a swirled burner at high amplitude combustion instabilities. *Journal of Engineering for Gas Turbines and Power* 2009; 131(5). DOI:10.1115/1.3078206.
- [10] Scarpato A, Tran N, Ducruix S et al. Modeling the damping properties of perforated screens traversed by a bias flow and backed by a cavity at low strouhal number. *Journal of Sound and Vibration* 2012; 331(2): 276–290. DOI:10.1016/j.jsv.2011.09.005.
- [11] Scarpato A, Ducruix S and Schuller T. Optimal and off-design operations of acoustic dampers using perforated plates backed by a cavity. *Journal of Sound and Vibration* 2013; 332(20): 4856–4875. DOI:10.1016/j.jsv.2013.03.030.
- [12] Scarpato A, Ducruix S and Schuller T. A comparison of the damping properties of perforated plates backed by a cavity operating at low and high strouhal numbers. *Comptes Rendus Mécanique* 2013; 341(1-2): 161–170. DOI:10.1016/j.crme.2012.10.016.
- [13] Lawn C. The acoustic impedance of perforated plates under various flow conditions relating to combustion chamber liners. *Applied Acoustics* 2016; 106: 144–154. DOI:10.1016/j.apacoust.2016.01.005.
- [14] Wu G, Li S, Zhao H et al. Experimental and frequency-domain study of acoustic damping of single-layer perforated plates. *Aerospace Science and Technology* 2017; 69: 432–438. DOI:10.1016/j.ast.2017.07.010.
- [15] Lahiri C and Bake F. A review of bias flow liners for acoustic damping in gas turbine combustors. *Journal of Sound and Vibration* 2017; 400: 564–605. DOI:10.1016/j.jsv.2017.04.005.
- [16] Meng S, Zhou H and Cen K. Application of the perforated plate in passive control of the nonpremixed swirl combustion instability under acoustic excitation. *Journal of Engineering for Gas Turbines and Power* 2019; 141(9). DOI:10.1115/1.4043848.
- [17] Zhou H, Liu Z, Tao C et al. Passive suppression of self-excited combustion instabilities in liquid spray flame using microperforated plate. *Journal of Engineering for Gas Turbines and Power* 2020; 142(11). DOI:10.1115/1.4047768.
- [18] Laurent C, Badhe A and Nicoud F. Representing the geometrical complexity of liners and boundaries in low-order modeling for thermoacoustic instabilities. *Journal of Computational Physics* 2021; 428: 110077. DOI:10.1016/j.jcp.2020.110077.
- [19] Allard J and Atalla N. *Propagation of Sound in Porous Media: Modelling Sound Absorbing Materials 2e*. New York: John Wiley & Sons, 2009. DOI:10.1002/9780470747339.
- [20] Douasbin Q, Scalo C, Selle L et al. Delayed-time domain impedance boundary conditions (D-TDIBC). *Journal of Computational Physics* 2018; 371: 50–66. DOI:10.1016/j.jcp.2018.05.003.

- [21] Rienstra S. Impedance models in time domain, including the extended Helmholtz resonator model. In *12th AIAA/CEAS Aeroacoustics Conference (27th AIAA Aeroacoustics Conference)*. p. 2686. DOI:10.2514/6.2006-2686.
- [22] Dragna D, Pineau P and Blanc-Benon P. A generalized recursive convolution method for time-domain propagation in porous media. *The Journal of the Acoustical Society of America* 2015; 138(2): 1030–1042. DOI:10.1121/1.4927553.
- [23] Monteghetti F, Matignon D, Piot E et al. Design of broadband time-domain impedance boundary conditions using the oscillatory-diffusive representation of acoustical models. *The Journal of the Acoustical Society of America* 2016; 140(3): 1663–1674. DOI:10.1121/1.4962277.
- [24] Diab D, Dragna D, Salze E et al. Nonlinear broadband time-domain admittance boundary condition for duct acoustics. application to perforated plate liners. *Journal of Sound and Vibration* 2022; 528: 116892. DOI:10.1016/j.jsv.2022.116892.
- [25] Roncen R and Cardesa JI. Generic and broadband nonlinear time domain impedance boundary condition. *Journal of Sound and Vibration* 2023; 554: 117691. DOI:10.1016/j.jsv.2023.117691.
- [26] Marchal T, Deniau H, Boussuge JF et al. Extension of the Spectral Difference method to premixed laminar and turbulent combustion. *Flow, Turbulence and Combustion* 2023; 111: 141–176. DOI:10.1007/s10494-023-00414-5.
- [27] Jones MG, Simon F and Roncen R. Broadband and Low-Frequency Acoustic Liner Investigations at NASA and ONERA. *AIAA Journal* 2021; : 1–20 DOI:10.2514/1.J060862.
- [28] Atalla N and Sgard F. Modeling of perforated plates and screens using rigid frame porous models. *Journal of sound and vibration* 2007; 303(1-2): 195–208. DOI:10.1016/j.jsv.2007.01.012.
- [29] Guess A. Calculation of perforated plate liner parameters from specified acoustic resistance and reactance. *Journal of Sound and Vibration* 1975; 40(1): 119–137. DOI:10.1016/S0022-460X(75)80234-3.
- [30] Melling TH. The acoustic impedance of perforates at medium and high sound pressure levels. *Journal of Sound and Vibration* 1973; 29(1): 1–65. DOI:10.1016/S0022-460X(73)80125-7.
- [31] American Society of Mechanical Engineers Digital Collection. *Comparison of various CFD codes for LES simulations of turbomachinery: from inviscid vortex convection to multi-stage compressor*, volume 2C: Turbomachinery, 2018.
- [32] Cassagne A, Boussuge J, Villedieu N et al. JAGUAR: a new CFD code dedicated to massively parallel high-order LES computations on complex geometry. In *The 50th 3AF International Conference on Applied Aerodynamics (AERO 2015)*.
- [33] Veilleux A, Puigt G, Deniau H et al. A stable Spectral Difference approach for computations with triangular and hybrid grids up to the 6th order of accuracy. *Journal of Computational Physics* 2021; : 110774 DOI:10.1016/j.jcp.2021.110774.
- [34] Veilleux A, Puigt G, Deniau H et al. Stable Spectral Difference Approach Using Raviart-Thomas Elements for 3D Computations on Tetrahedral Grids. *Journal of Scientific Computing* 2022; 91(1): 1–22. DOI:10.1007/s10915-022-01790-2.
- [35] Fiévet R, Deniau H and Piot E. Strong compact formalism for characteristic boundary conditions with discontinuous spectral methods. *Journal of Computational Physics* 2020; 408: 109276. DOI:10.1016/j.jcp.2020.109276.
- [36] Kopriva D. A staggered-grid multidomain spectral method for the compressible Navier–Stokes equations. *Journal of Computational Physics* 1998; 143(1): 125–158. DOI:10.1006/jcph.1998.5956.
- [37] Poinso T and Veynante D. *Theoretical and numerical combustion*. Philadelphia, PA: RT Edwards, Inc., 2005.
- [38] Stull D and Prophet H. JANAF Thermochemical Tables. *National Standard Reference Data Series, Nat Bur Stds(US), IL* 1971; 1141.
- [39] Sun Y, Wang ZJ and Liu Y. High-order multidomain Spectral Difference method for the Navier-Stokes equations on unstructured hexahedral grids. *Communications in Computational Physics* 2007; 2(2): 310–333. DOI:10.2514/6.2006-301.
- [40] Van den Abeele K, Lacor C and Wang Z. On the stability and accuracy of the spectral difference method. *Journal of Scientific Computing* 2008; 37(2): 162–188. DOI:10.1007/s10915-008-9201-0.
- [41] Jameson A. A proof of the stability of the spectral difference method for all orders of accuracy. *Journal of Scientific Computing* 2010; 45(1-3): 348–358. DOI:10.1007/s10915-009-9339-4.
- [42] Toro EF. *Riemann solvers and numerical methods for fluid dynamics: a practical introduction*. Springer Science & Business Media, 2013.
- [43] Batten P, Clarke N, Lambert C et al. On the choice of wavespeeds for the HLLC Riemann solver. *Journal of Scientific Computing* 1997; 18(6): 1553–1570. DOI:10.1137/S1064827593260140.
- [44] Gottlieb S and Shu CW. Total variation diminishing Runge-Kutta schemes. *Mathematics of Computation* 1998; 67(221): 73–85.
- [45] Franzelli B, Riber E, Sanjosé M et al. A two-step chemical scheme for kerosene–air premixed flames. *Combustion and Flame* 2010; 157(7): 1364–1373. DOI:10.1016/j.combustflame.2010.03.014.
- [46] Poinso TJ and Lelef S. Boundary conditions for direct simulations of compressible viscous flows. *Journal of computational physics* 1992; 101(1): 104–129. DOI:10.1016/0021-9991(92)90046-2.
- [47] Ghani A, Poinso T, Gicquel L et al. LES of longitudinal and transverse self-excited combustion instabilities in a bluff-body stabilized turbulent premixed flame. *Combustion and Flame* 2015; 162(11): 4075–4083. DOI:10.1016/j.combustflame.2015.08.024.